

## Bottom-simulating reflectors: Seismic velocities and AVO effects

José M. Carcione\* and Umberta Tinivella\*

### ABSTRACT

We obtain the wave velocities of ice- and gas hydrate-bearing sediments as a function of concentration and temperature. Unlike previous theories based on simple slowness and/or moduli averaging or two-phase models, we use a Biot-type three-phase theory that considers the existence of two solids (grain and ice or clathrate) and a liquid (water), and a porous matrix containing gas and water.

For consolidated Berea sandstone, the theory underestimates the value of the compressional velocity below 0°C. Including grain-ice interactions and grain cementation yields a good fit to the experimental data. Strictly speaking, water proportion and temperature are closely related. Fitting the wave velocity at a given temperature allows the prediction of the velocity throughout the range of temperatures, provided that the average pore radius and its standard deviation are known.

The reflection coefficients are computed with a viscoelastic single-phase constitutive model. The analysis is carried out for the top and bottom of a free-gas zone beneath a gas hydrate-bearing sediment and overlying a sediment fully saturated with water. Assuming that the bottom-simulating reflector is caused solely by an interface separating cemented gas hydrate- and free gas-bearing sediments, we conclude that (1) for a given gas saturation, it is difficult to evaluate the amount of gas hydrate at low concentrations. However, low and high concentrations of hydrate can be distinguished, since they give positive and negative anomalies, respectively. (2) Saturation of free gas can be determined from the reflection amplitude, but not from the type of anomaly. (3) The  $P$  to  $S$  reflection coefficient is a good indicator of high amounts of free gas and gas hydrate. On the other hand, the amplitude-variation-with-offset curves are always positive for uncemented sediments.

### INTRODUCTION

Gas hydrate is a clathrate composed of water and natural gas, mainly methane, which forms under conditions of low temperature, high pressure, and proper gas concentration. Bottom-simulating reflectors (BSRs) on seismic profiles are interpreted to represent the seismic signature of the base of gas hydrate formation; a free gas zone may be present just below the BSR (e.g., Andreassen et al., 1990).

Where no direct measurements are available, detailed knowledge of the compressional and/or shear wave velocity distribution in marine sediments is essential for quantitative estimates of gas hydrate and free gas in the pore space. The discrepancies between the inverted velocity profile (from seismic data) and the velocity for water-filled, normally compacted marine sediments are interpreted as caused by the presence of gas hydrate (where positive anomalies are present) and free gas (where negative anomalies are present). These anomalies can be translated in terms of concentration of clathrate and free gas if the velocity trend versus gas hydrate and free gas content is

known. An alternative method for estimating the amount of hydrate and gas is to analyze the variation of the reflection coefficient of the BSR versus offset.

The elastic properties of ice are similar to those of hydrate, so the properties of permafrost are often compared with those of hydrated sediments (Sloan, 1990). Timur (1968) proposed a three-phase time-average equation based on slowness averaging (Wyllie's equation) for modeling consolidated permafrost sediments. Moreover, he found that as temperature is decreased below 0°C, the water contained in the large pores freezes first, and that the freezing process ends between -21°C and -22°C, in accordance with the phase diagram for the sodium chloride-water system. The problem of transition from "suspension" to "compacted" sediment was treated with combined models. For instance, averaging bulk moduli weighted with the respective porosities [Voigt's model (Voigt, 1928)] gives a simple model for consolidated sediments, whereas averaging the reciprocal of bulk moduli [Reuss's model (Reuss, 1929)] accounts for unconsolidated media. Zimmerman and

Manuscript received by the Editor December 04, 1997; revised manuscript received December 15, 1998.  
\*Osservatorio Geofisico Sperimentale, Borgo Grotta Gigante 42c, 34010 Sgonico, Trieste, Italy. E-mail: jcarcione@ogs.trieste.it; utinivella@ogs.trieste.it.  
© 2000 Society of Exploration Geophysicists. All rights reserved.

King (1986) used the two-phase theory developed by Kuster and Toksöz (1974), assuming that unconsolidated permafrost can be approximated by an assemblage of spherical quartz grains embedded in a matrix composed of spherical inclusions of water and ice. They first compute the effective elastic moduli of the ice-water mixture, with water playing the role of inclusion. This yields a homogeneous medium where the sand grains are the inclusion.

A three-phase theory based on first principles was proposed by Leclaire et al. (1994). The theory, hereafter called as the LCA model, assumes that there is no direct contact between solid grains and ice since, in principle, water tends to form a thin film around the grains. The theory predicts three compressional waves and two shear waves, and can be applied to unconsolidated and consolidated media. Leclaire et al. (1994) also provide a thermodynamic relation between the water proportion and temperature. On the other hand, Santos et al. (1990a, b) presented a theory describing wave propagation in a porous medium saturated with a mixture of two immiscible, viscous, compressible fluids. We use this theory for calculating the wave velocities of sediments partially saturated with gas and water. Therefore, the BSR is modeled by a porous medium in which there are two solid components (matrix and gas hydrates) overlying a gas- and water-filled porous medium having the same solid skeleton as the upper medium.

### MODEL FOR GAS HYDRATE-BEARING SEDIMENTS

The theory developed by Leclaire et al. (1994) explicitly takes into account the presence of the three phases. Here, we have included the contributions to the potential and kinetic energies due to the contact between the solid grains and the hydrates, and the stiffening of the skeleton due to grain cementation. In fact, samples of gas hydrate recovered in a well (ODP Leg 164 Shipboard Scientific Party, 1996) and a real data study (Ecker et al., 1996) suggest that the hydrates are distributed through the pore space and across the grains.

The equation of motion of the modified LCA model (LCAM) can be written in matrix form as

$$\mathbf{R} \operatorname{grad} \operatorname{div} \mathbf{u} - \boldsymbol{\mu} \operatorname{curl} \operatorname{curl} \mathbf{u} = \tilde{\rho} \ddot{\mathbf{u}} + \mathbf{A} \dot{\mathbf{u}},$$

where  $\mathbf{u}$  is the displacement field,

$$\mathbf{R} = \begin{pmatrix} R_{11} & R_{12} & R_{13} \\ R_{12} & R_{22} & R_{23} \\ R_{13} & R_{23} & R_{33} \end{pmatrix} \quad \text{and} \quad \boldsymbol{\mu} = \begin{pmatrix} \mu_{11} & 0 & \mu_{13} \\ 0 & 0 & 0 \\ \mu_{13} & 0 & \mu_{33} \end{pmatrix}$$

are the stiffness and shear matrices,

$$\tilde{\rho} = \begin{pmatrix} \tilde{\rho}_{11} & \tilde{\rho}_{12} & \tilde{\rho}_{13} \\ \tilde{\rho}_{12} & \tilde{\rho}_{22} & \tilde{\rho}_{23} \\ \tilde{\rho}_{13} & \tilde{\rho}_{23} & \tilde{\rho}_{33} \end{pmatrix}$$

is the mass density matrix, and

$$\mathbf{A} = \begin{pmatrix} b_{11} & -b_{11} & 0 \\ -b_{11} & b_{11} + b_{33} & -b_{33} \\ 0 & -b_{33} & b_{33} \end{pmatrix}$$

is the friction matrix, where  $b_{13}$  have been assumed equal to zero (this parameter describes solid-grain/hydrate friction). A

dot above a variable denotes time differentiation. All the parameters with the subindex (13) describe the interaction between the two solid components.

An effective density  $\rho = \tilde{\rho} - i\mathbf{A}/\omega$  can be defined in the frequency domain.

The three compressional velocities of the three-phase frozen porous medium are given by

$$V_{Pi} = [\operatorname{Re}(\sqrt{\Lambda_i})]^{-1}, \quad i = 1, \dots, 3, \quad (1)$$

where  $\operatorname{Re}$  takes the real part and  $\Lambda_i$  are obtained from the following characteristic equations:

$$\begin{aligned} \Lambda^3 \det(\mathbf{R}) - \Lambda^2 a + \Lambda b - \det(\boldsymbol{\rho}) &= 0, \\ \det(\mathbf{R}) &= R_{11} R_{22} R_{33} - R_{23}^2 R_{11} - R_{12}^2 R_{33} - R_{13}^2 R_{22} \\ &\quad + 2R_{12} R_{23} R_{13}, \\ a &= a_1 + a_2 + a_3, \\ a_1 &= \rho_{11} \det(R_{iw}) + \rho_{22} \det(R_{si}) + \rho_{33} \det(R_{sw}), \\ a_2 &= -2(\rho_{23} R_{23} R_{11} + \rho_{12} R_{12} R_{33} + \rho_{13} R_{13} R_{22}), \\ a_3 &= 2(\rho_{23} R_{13} R_{12} + \rho_{13} R_{12} R_{23} + \rho_{12} R_{23} R_{13}), \\ \det(R_{sw}) &= R_{11} R_{22} - R_{12}^2, \\ \det(R_{iw}) &= R_{22} R_{33} - R_{23}^2, \\ \det(R_{si}) &= R_{11} R_{33} - R_{13}^2, \\ \det(\boldsymbol{\rho}) &= \rho_{11} \rho_{22} \rho_{33} - \rho_{23}^2 \rho_{11} - \rho_{12}^2 \rho_{33} - \rho_{13}^2 \rho_{22} \\ &\quad + 2\rho_{12} \rho_{23} \rho_{13}, \\ \det(\rho_{sw}) &= \rho_{11} \rho_{22} - \rho_{12}^2, \\ \det(\rho_{iw}) &= \rho_{22} \rho_{33} - \rho_{23}^2, \\ \det(\rho_{si}) &= \rho_{11} \rho_{33} - \rho_{13}^2, \\ b &= b_1 + b_2 + b_3, \\ b_1 &= R_{11} \det(\rho_{iw}) + R_{22} \det(\rho_{si}) + R_{33} \det(\rho_{sw}), \\ b_2 &= -2(R_{23} \rho_{23} \rho_{11} + R_{12} \rho_{12} \rho_{33} + R_{13} \rho_{13} \rho_{22}), \\ b_3 &= 2(R_{23} \rho_{13} \rho_{12} + R_{13} \rho_{12} \rho_{23} + R_{12} \rho_{23} \rho_{13}). \end{aligned}$$

The two shear velocities  $V_{Si}$  are given by

$$V_{Si} = [\operatorname{Re}(\sqrt{\Omega_i})]^{-1}, \quad i = 1, 2 \quad (2)$$

where  $\Omega_i$  are the complex solutions of the equation

$$\begin{aligned} \Omega^2 a' - \Omega b' + \det(\boldsymbol{\rho}) &= 0, \\ a' &= \rho_{22} \det(\mu_{si}), \\ b' &= \mu_{11} \det(\rho_{iw}) + \mu_{33} \det(\rho_{sw}) \\ &\quad - 2\mu_{13} \rho_{13} \rho_{22} + 2\mu_{13} \rho_{12} \rho_{23}, \\ \det(\mu_{si}) &= \mu_{11} \mu_{33} - \mu_{13}^2. \end{aligned}$$

Appendix A illustrates the meaning of the different parameters, and Appendix B the generalization of the potential and kinetic energies. The expressions for  $K_{\max}$  and  $\mu_{\max}$  can be found in Zimmerman and King [1986, equations (1) and (2), respectively], with the subscript  $m$  corresponding to ice,  $i$  corresponding to air, and the concentration  $c$  equal to  $\phi_s$ . They are the moduli of the ice matrix, with the water totally frozen and the solid replaced by air. On the other hand, we assume that the rigidity modulus of the solid matrix  $\mu_{sm}$  is affected by cementation of the sand grains by ice. The equation, indicated

in Appendix A, follows the same percolation model used for the ice matrix (Leclaire et al., 1994). The rigidity  $\mu_{sm0}$  is the shear modulus of the rock at full water saturation. Alternatively, the cementation effect can be introduced through the coupling modulus  $\hat{\mu}_{si}$  by means of a similar percolation model. In this work, we assume  $\hat{\mu}_{si} = 0$ .

The expressions for the density components, given in Appendix B, include the interaction between the grain and ice phases, assuming that the grains flow through the ice matrix (described by the tortuosity  $a_{13}$ ) and the ice flows through the skeleton (described by  $a_{31}$ ). As is well known, the tortuosity is related to the difference between the microvelocity and macrovelocity fields. If they are similar (i.e., for relatively rigid materials like solids), the tortuosities equal 1 and the contributions vanish. However, we assume that these terms contribute to the kinetic energy when the solid and ice matrices are unconsolidated or relatively unconsolidated, for which the tortuosities are greater than 1. As in Biot theory, we neglect the solid contributions related to the interaction with water.

On the other hand, depending on the frequency, a very thin and viscous water layer may transmit shear deformations from one matrix to the other. In this case, the coefficients  $\mu_1$ ,  $\mu_2$ , and  $\mu_{13}$  become relaxation functions and should be replaced (in the time domain) by the operators  $\mu_1*$ ,  $\mu_2*$ , and  $\mu_{13}* (*$  denotes time convolution), with  $\mu_{av}$  representing a Maxwell mechanical model with two springs, whose stiffnesses are  $\mu_s/(1-g_1)\phi_s$  and  $\mu_i/(1-g_3)\phi_i$ , and a dashpot of viscosity  $\eta_w/\phi_w$ . Note that Leclaire et al. (1994) neglect the imaginary part of the Maxwell complex modulus, and then the related attenuation effects.

Assuming a Gaussian porosimetric distribution, the water proportion  $\phi_w$  can be obtained as a function of temperature as

$$\phi_w = (1 - \phi_s) A \int_0^{r_0/\ln(T_0/T)} \exp[-(r - r_{av})^2/(2\Delta r^2)] dr, \quad (3)$$

where  $r_{av}$  is the average pore radius,  $\Delta r$  is the standard deviation, and the temperature  $T$  is given in Kelvins and  $T_0 = 273$  K (Hudson, 1992; Leclaire et al., 1994). The quantity  $r_0 = 0.228$  nm in the ideal case, but here it is used as a parameter in order to take into account the salinity content of the pore water. As stated by Timur (1968), as the ice crystallizes out as pure water, the sodium chloride concentration of the remaining solution increases, thereby further lowering the freezing point. Hence, ice may be thought of as forming on the walls of the larger pores and growing into the pore spaces. This effect is modeled by equation (3).

The constant  $A$  is obtained after normalization of the Gaussian probability function from  $r=0$  to  $r=\infty$ . Thus, we obtain

$$\phi_w = (1 - \phi_s) \frac{\operatorname{erf}(\zeta) + \operatorname{erf}(\eta)}{1 + \operatorname{erf}(\eta)}, \quad \zeta = \frac{r_0/\ln(T_0/T)}{\sqrt{2}\Delta r} - \eta, \\ \eta = \frac{r_{av}}{\sqrt{2}\Delta r}. \quad (4)$$

#### MODEL FOR FREE GAS-BEARING SEDIMENTS

The porous media saturated by a mixture of water and free gas can be described by the theory developed by Santos et al.

(1990a, b). The velocity of compressional waves is

$$V_P = \left[ \operatorname{Re} \left( \frac{1}{V} \right) \right]^{-1}, \quad (5)$$

where  $V$  is the complex velocity satisfying the eigenvalue equation

$$\mathbf{M}\mathbf{q} = V^2(\mathbf{D} - i\mathbf{L})\mathbf{q}, \quad (6)$$

with  $\mathbf{q}$  the eigenvectors,

$$\mathbf{M} = \begin{pmatrix} K_c & B_1 & B_2 \\ B_1 & M_1 & M_3 \\ B_2 & M_3 & M_2 \end{pmatrix} \text{ and } \mathbf{D} = \begin{pmatrix} \rho & \rho_g S_g & \rho_w S_w \\ \rho_g S_g & \bar{g}_1 & \bar{g}_3 \\ \rho_w S_w & \bar{g}_3 & \bar{g}_2 \end{pmatrix}$$

the stiffness and density matrices, respectively, and

$$\mathbf{L} = \operatorname{diag} \left( 0, \frac{S_g^2 \bar{\eta}_g}{\omega \kappa_g}, \frac{S_w^2 \bar{\eta}_w}{\omega \kappa_w} \right)$$

the friction matrix. The shear velocity is

$$V_S = \left[ \operatorname{Re} \left( \frac{1}{V} \right) \right]^{-1}, \quad (7)$$

where

$$V = \sqrt{\mu_{sm0}} \left[ \rho_m - \frac{\rho_g S_g (g_2^* \rho_g S_g - \bar{g}_3 \rho_w S_w) + \rho_w S_w (g_1^* \rho_w S_w - \bar{g}_3 \rho_g S_g)}{g_1^* g_2^* - \bar{g}_3^2} \right]$$

and

$$g_1^* = \bar{g}_1 - i \frac{S_g^2 \bar{\eta}_g}{\omega \kappa_g}, \quad \text{and} \quad g_3^* = \bar{g}_3 - i \frac{S_w^2 \bar{\eta}_w}{\omega \kappa_w}.$$

The permeabilities can be expressed as

$$\kappa_g = \kappa_{s0} k_{rg} \quad \text{and} \quad \kappa_w = \kappa_{s0} k_{rw},$$

where  $k_{rg}$  and  $k_{rw}$  are the relative permeabilities.

For low frequencies (i.e., the seismic case), the compressional and shear velocities are

$$V_P = \sqrt{(K_c + 4\mu_{sm0}/3)/\rho_m}, \quad \text{and} \quad V_S = \sqrt{\mu_{sm0}/\rho_m} \quad (8)$$

(see Appendix A for more details).

#### WAVE VELOCITIES OF BEREAL SANDSTONE

The first example (see Figure 1) compares the compressional velocity obtained by using the present theory with those of the most common acoustic models for permafrost. A description of these models can be found, for instance, in Carcione and Seriani (1998). The data (see Table 1) correspond to Berea sandstone, with the properties given by Timur (1968) and Winkler (1985). The Voigt and Wood models provide upper and lower bounds for the bulk and rigidity moduli. Roughly, the velocities of the different models must lie between the Voigt and Wood velocities (note that the bounds refer to the moduli, not to the velocities). The time average velocity is obtained by averaging the slowness of the different phases weighted by the respective porosities. Minshull et al. (1994) obtain an effective

medium 1 by time averaging the solid and ice (gas-hydrate) phases; then, they obtain a medium 2 for the water-filled sediment from Gassmann's equation; finally, they time average mediums 1 and 2 to obtain the velocity of the partially saturated sediment. On the other hand, Zimmerman and King (1986) use Kuster and Toksöz's (1974) theory for obtaining the effective moduli of the ice-water mixture (with water playing the role of inclusion), and then use this mixture as a background medium where the sand grains are the inclusion. This gives an unconsolidated model for permafrost, with low velocities for low ice concentrations.

The curves LCA, LCAM and M (Minshull et al., 1994) coincide and give Biot's results at full water saturation, but they give different values at full ice saturation. Note that the cementation effect is strong for high concentrations of ice (compare the LCA and LCAM curves). The curve ZK (Zimmerman and King, 1986) coincides with Wood's model (W) at full water saturation, since it assumes an unconsolidated matrix. All the theories correctly predict the behavior of the fast wave velocity in a partially frozen medium, i.e., velocity decreases for increasing water saturation. Finally, the V (Voigt's model) curve seems to overestimate the velocity.

The next example (Figure 2) analyzes the dependence of the compressional velocity of permafrost on temperature. The data (see Table 1) correspond to Berea sandstone, with the properties given by Timur (1968) and Winkler (1985). In order to evaluate the influence of ice-grain interactions and grain cementation, we represent the compressional and shear velocities versus ice concentration corresponding to four different models. As can be appreciated, cementation, modeled by the percolation theory, is the most important

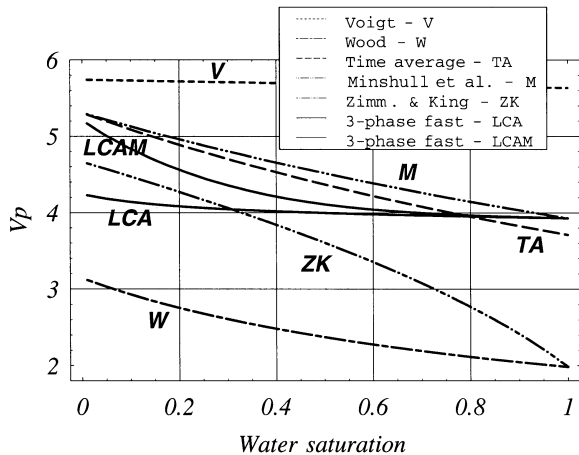


FIG. 1. Compressional wave velocity versus water proportion predicted by the different theories. The medium is Berea sandstone, whose properties are given in Table 1. LCAM is the modified theory.

factor. However, for low concentrations (less than 30%), all velocities coincide in practice.

Figure 3a shows the water proportion  $\phi_w$  as a function of temperature computed from equation (4), assuming  $r_{av} = 10 \mu\text{m}$ ,  $\Delta r = 10 \mu\text{m}$ , and  $r_0 = 0.04 \mu\text{m}$ . Figure 3b represents the compressional wave velocity versus temperature, where the squares correspond to the experimental data measured by Timur (1968). The sample was subjected to an uniaxial pressure of 313 atm, and the pore fluid was under atmospheric pressure. The sample, with a porosity of 0.2, was first cooled to  $-23^\circ\text{C}$ , and then brought back to room temperature. Two curves, computed at 200 kHz, are fitted to the experimental points. The dotted curve strictly corresponds to Leclaire et al.'s (1994) theory, i.e., grain-ice interactions and grain cementation with decreasing temperature are not taken into account, and assuming  $r_{av} = 10 \mu\text{m}$ ,  $\Delta r = 4 \mu\text{m}$ , and  $r_0 = 0.228 \text{ nm}$  (pure water). As can be seen, the velocity is underestimated below  $0^\circ\text{C}$ . The continuous line, which fits the data fairly well, was obtained from the present model.

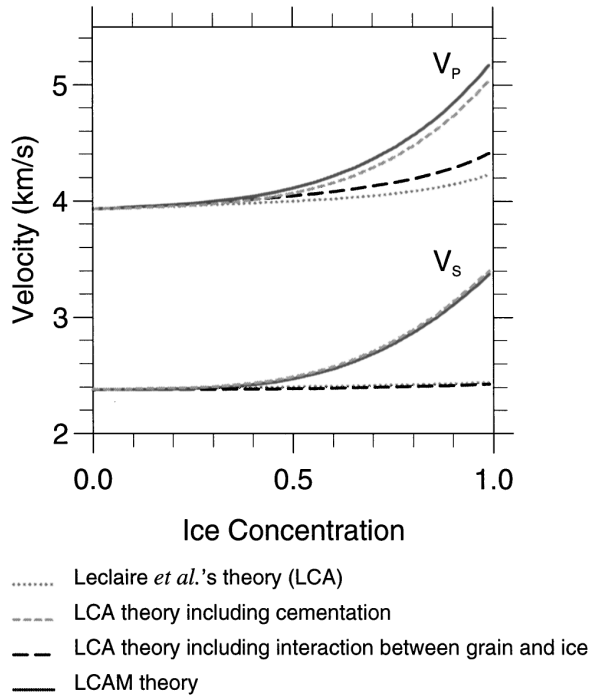


FIG. 2. Compressional and shear velocities for an ice-bearing sediment (Berea sandstone, see Table 1) versus ice concentration, corresponding to the original theory developed by Leclaire et al. (1994) (LCA, dotted line), to the theory including cementation (broken line), to the theory including grain-ice contact (light broken line), and to the LCAM model (continuous line). The frequency is 25 Hz.

Table 1. Material properties for frozen Berea sandstone.

Grain	$\rho_s = 2650 \text{ kg/m}^3$	$K_s = 38.7 \text{ GPa}$	$\mu_s = 39.6 \text{ GPa}$	$\kappa_{s0} = 1.07 \cdot 10^{-13} \text{ m}^2$
Ice	$\rho_i = 920 \text{ kg/m}^3$	$K_i = 8.58 \text{ GPa}$	$\mu_i = 3.7 \text{ GPa}$	$\kappa_{i0} = 5 \times 10^{-4} \text{ m}^2$
Water	$\rho_w = 1000 \text{ kg/m}^3$	$K_w = 2.25 \text{ GPa}$	$\mu_w = 0 \text{ GPa}$	$\bar{\eta}_w = 1.798 \text{ cP}^*$
$K_{sm} = 14.4 \text{ GPa}$	$\mu_{sm0} = 13.1 \text{ GPa}$	$r_s = 50 \mu\text{m}$	$r_{av} = 10 \mu\text{m}$	$\Delta r = 10 \mu\text{m}$
<sup>*</sup> 1 cP = 0.001 Pa·s.				

### REFLECTION AND TRANSMISSION COEFFICIENTS

The properties of the sediment and of its individual constituents causing the BSR are given in Table 2. The compressional and shear velocities at 25 Hz versus gas hydrate and free-gas saturations are represented in Figures 4a and 4b, respectively. At zero saturation these velocities coincide with

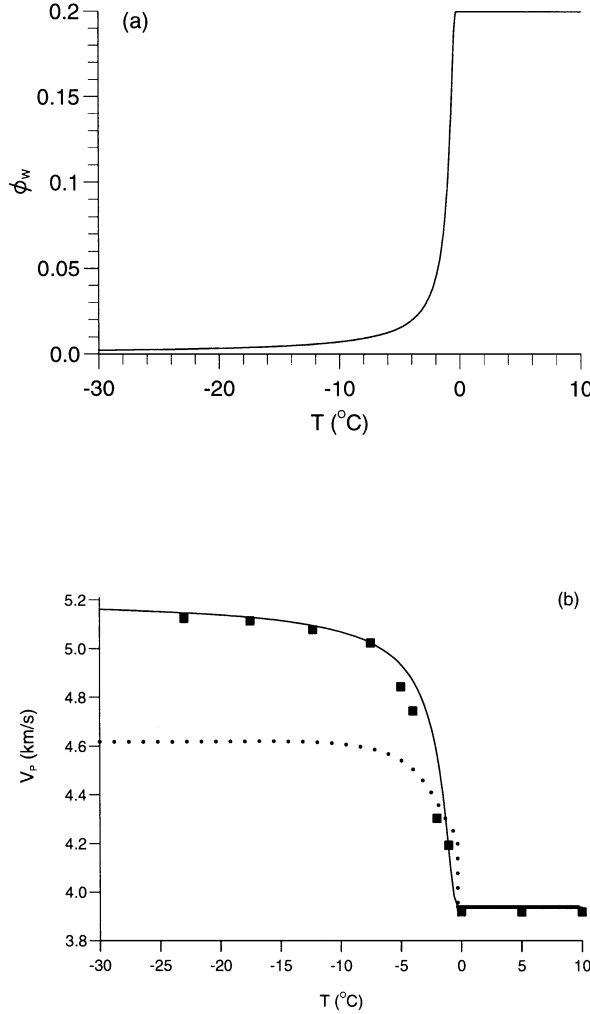


FIG. 3. (a) Water proportion  $\phi_w$  as a function of temperature. (b) Compressional wave velocity versus temperature in (consolidated) Berea sandstone at 200 kHz. The squares correspond to the experimental data measured by Timur (1968), and the dotted curve to the theory developed by Leclaire et al. (1994) (LCA model).

Table 2. Material properties for hydrate- and free gas-bearing sediments.

Grain	$\rho_s = 2650 \text{ kg/m}^3$	$K_s = 38.7 \text{ GPa}$	$\mu_s = 39.6 \text{ GPa}$	$\kappa_{s0} = 1.07 \times 10^{-13} \text{ m}^2$
Gas hydrate	$\rho_h = 920 \text{ kg/m}^3$	$K_h = 8.27 \text{ GPa}$	$\mu_h = 3.39 \text{ GPa}$	$\kappa_{i0} = 5 \times 10^{-4} \text{ m}^2$
Water	$\rho_w = 1030 \text{ kg/m}^3$	$K_w = 2.39 \text{ GPa}$	$\mu_w = 0 \text{ GPa}$	$\bar{\eta}_w = 1.798 \text{ cP}$
Gas	$\rho_g = 116 \text{ kg/m}^3$	$K_g = 0.0236 \text{ GPa}$	$\mu_g = 0 \text{ GPa}$	$\bar{\eta}_g = 0.01 \text{ cP}$
$K_{sm} = 1.095 \text{ GPa}$	$\mu_{sm0} = 1.19 \text{ GPa}$	$r_s = 50 \mu\text{m}$	$1 - \phi_s = 0.4$	$r_{12} = 0.5$
$r_{13} = 0.5$	$r_{23} = 0.5$	$r_{31} = 0.5$	$k_{rw} = 0.04$	$k_{rg} = 0.4$

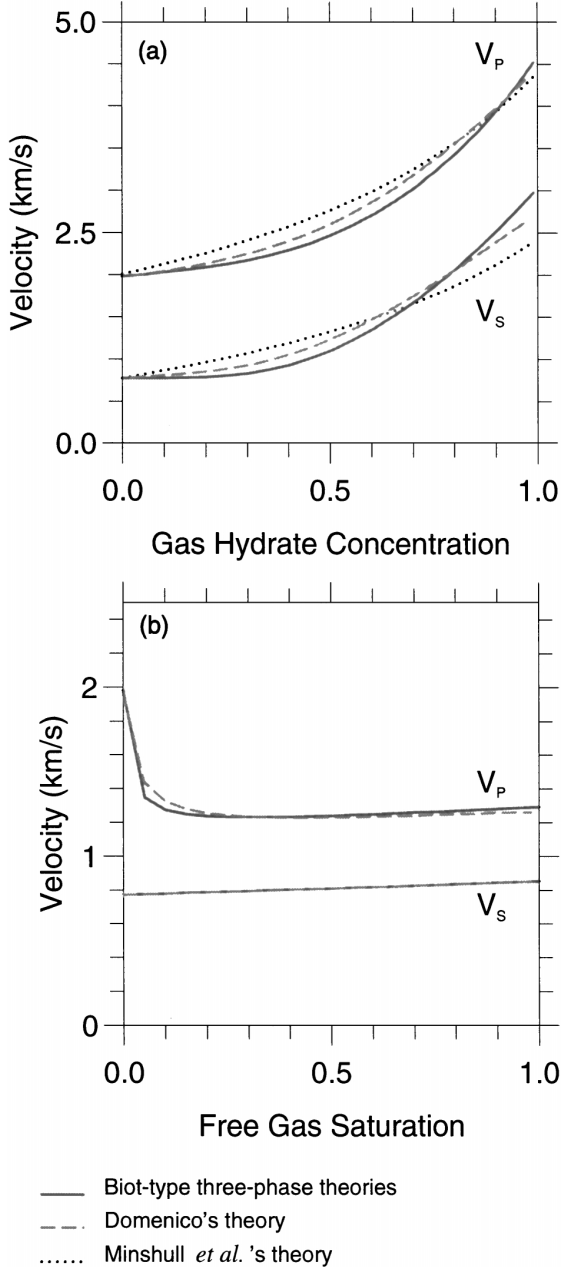


FIG. 4. Seismic compressional (a) and shear (b) velocities for a gas hydrate-bearing sediment (see Table 2) as a function of gas hydrate concentration, corresponding to the LCAM model (continuous line), Domenico's (1977) model (broken line), and Minshull et al.'s (1994) model (dotted line).

those of Biot's theory. On the other hand, Figure 5 displays the respective Poisson ratios. Also illustrated are the velocities and Poisson's ratios obtained with Domenico's theory (Domenico, 1977) and Minshull et al.'s (1994) model. Actually, Minshull

et al. assumed a linear decrease of the Poisson ratio from 0.41 to 0.28 with increasing hydrate concentration. The modified LCA model gives a nearly constant Poisson's ratio for low concentrations and a rapidly decreasing one for high concentrations.

The BSR is assumed to be a layer partially saturated with free gas beneath a hydrate-bearing sediment and overlying a sediment fully saturated with water. Our objective here is to study the reflection and transmission coefficients of the top and bottom of the free gas zone. These are calculated by first computing the wave velocities from the three-phase theories and then using a single phase model that includes attenuation effects (e.g., Carcione, 1997). The anelasticity is described by two standard linear solid elements associated with dilatational and shear deformations, where the relaxation times are expressed as a function of the respective minimum quality factors  $Q_1$  and  $Q_2$ , and the center frequency  $f_0$  of the relaxation peaks. It is important to point out here that by using a single-phase model for computing the reflection coefficients, we ignore the presence of two additional compressional waves and a second shear wave, whose velocities are represented in Figure 6 ( $V_{P2}$ ,  $V_{P3}$ , and  $V_{S2}$ , respectively). Moreover, this approximation neglects conversion between the different phases.

Amplitude variation with offset (AVO) variations for various models corresponding to the top of the BSR are displayed in Figure 7. We assume that the quality factors of the hydrate-bearing sediments are  $Q_1 = Q_2 = 30$ , and those of the free gas-bearing sediments are  $Q_1 = Q_2 = 20$ . The AVO anomalies can be of type II, III, and IV according to the classification given by Castagna and Swan (1997). We recall that for type II anomalies the amplitude may increase or decrease with offset (there is a change of sign in the reflection coefficient), for type III anomalies the reflection coefficient is negative and its absolute value increases with offset, and for type IV anomalies the coefficient is negative and its absolute value decreases with offset. Here, the anomalies are class IV for very high concentrations of gas hydrate, and classes II and III for relatively low concentrations. As stated by Minshull et al. (1994), for low saturations, the behavior is quite different in the presence and in the absence of free gas. Increasing free gas saturation causes an increase in the magnitude of the reflection coefficient with increasing offset. However, for a given gas saturation, it is difficult to evaluate the amount of gas hydrate at low saturations.

Ecker et al. (1996) show, from an AVO analysis and a rock physics model, that gas hydrate-bearing sediments from the Blake Outer Ridge (offshore Florida and Georgia) seem to be uncemented. In order to evaluate the influence of this factor on the reflection amplitudes, we represent in Figure 8 the curves corresponding to Figure 7, but without grain cementation. The curves are similar for low concentrations but differ for high concentrations. In this case, the AVO anomaly is always positive.

Figures 9 and 10 represent the reflection coefficients  $R_{PP}$  and  $R_{PS}$  at 25 Hz for various saturations. In part (a) each figure, the hydrate concentration is fixed at 10%, and in part (b) of each figure the free gas saturation is fixed at 10%. According to Figure 9, the free gas saturation can be determined from reflection amplitude but not from the type of anomaly. Moreover, the gas hydrate content can be determined when the concentration is high. On the other hand,  $R_{PS}$  is a good indicator of high amounts of free gas and gas hydrate.

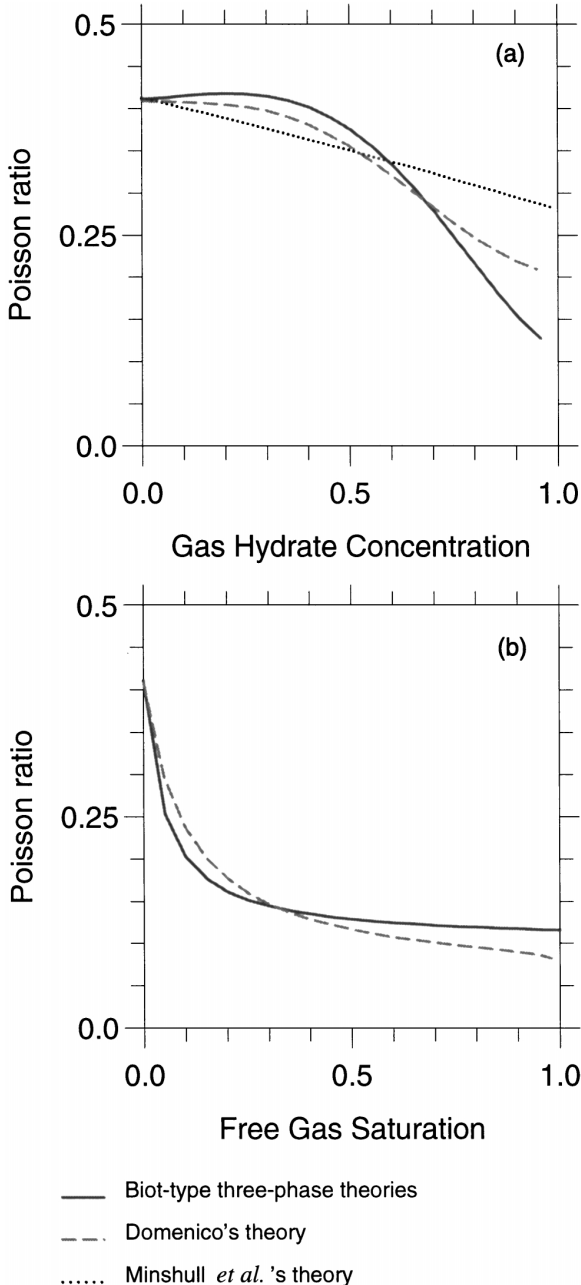


FIG. 5. Seismic Poisson ratios for a gas hydrate-bearing sediment (a) and a free gas-bearing sediment (b) as a function of the respective saturations. They are given for the LCAM model (continuous line) and Domenico's (1977) model (broken line). The dotted line in (a) is the Poisson ratio assumed by Minshull et al. (1994) in their analysis.

Figure 11 shows common-midpoint (CMP) gathers of the vertical particle velocity corresponding to the top of the BSR with 10% gas hydrate and 0%, 1%, and 20% free gas. The material properties are given in Table 3, and the previous quality factors are assumed. The source is a 25-Hz Ricker wavelet located 520 m above the BSR. As predicted by the theoretical curves, small quantities of gas in the pore space cause a dramatic change in the amplitude of the compressional wave.

**Table 3. Material properties.**

Medium	$V_P$ (m/s)	$V_S$ (m/s)	$\rho$ (kg/m <sup>3</sup> )
10% hydrate	2030	773	1998
0% free gas	1982	771	2002
1% free gas	1641	772	1998
20% free gas	1236	785	1928

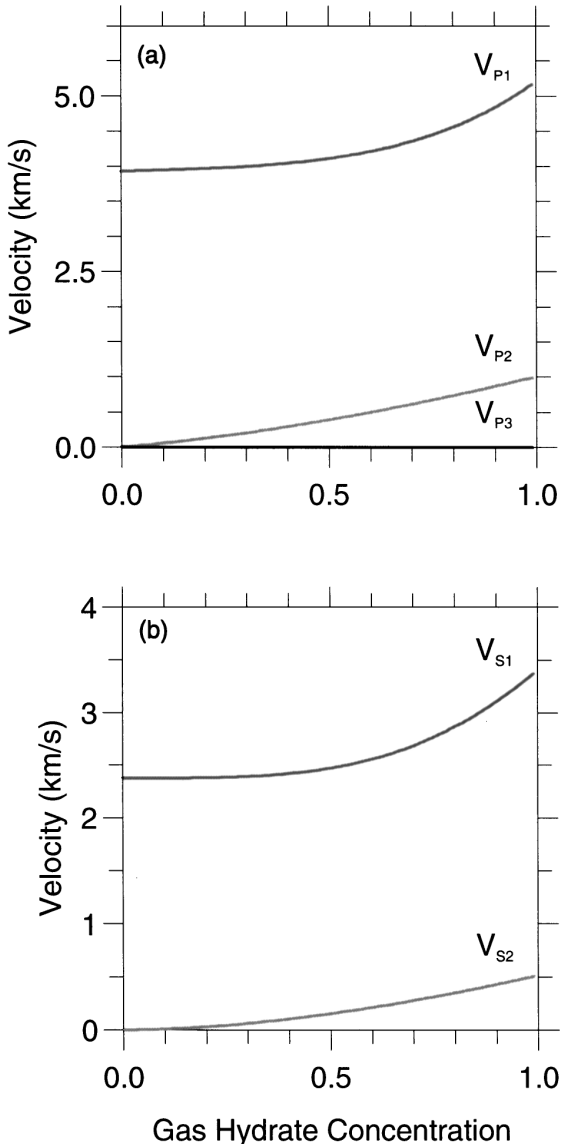


FIG. 6. Velocities of the additional compressional waves (a) and second shear wave (b).

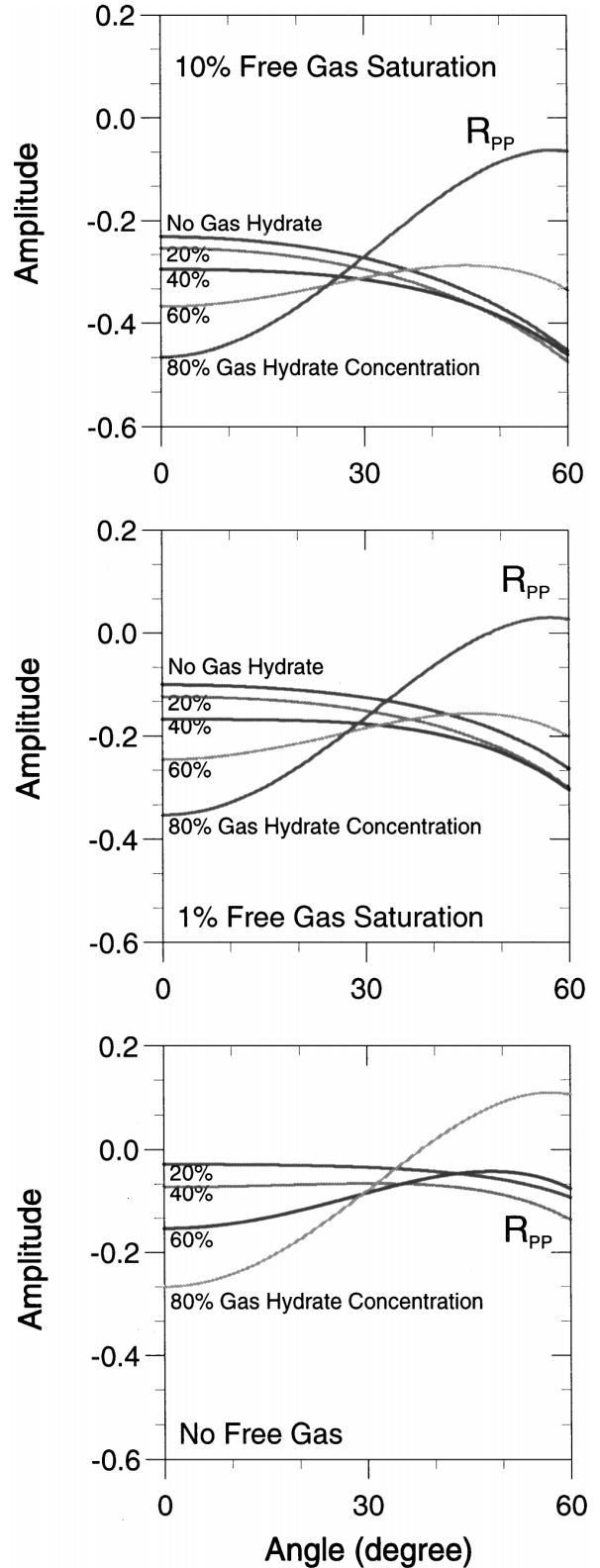


FIG. 7. Variations of BSR PP-wave viscoelastic reflection coefficient with angle of incidence for different free-gas and gas-hydrate saturations (LCAM model with grain cementation).

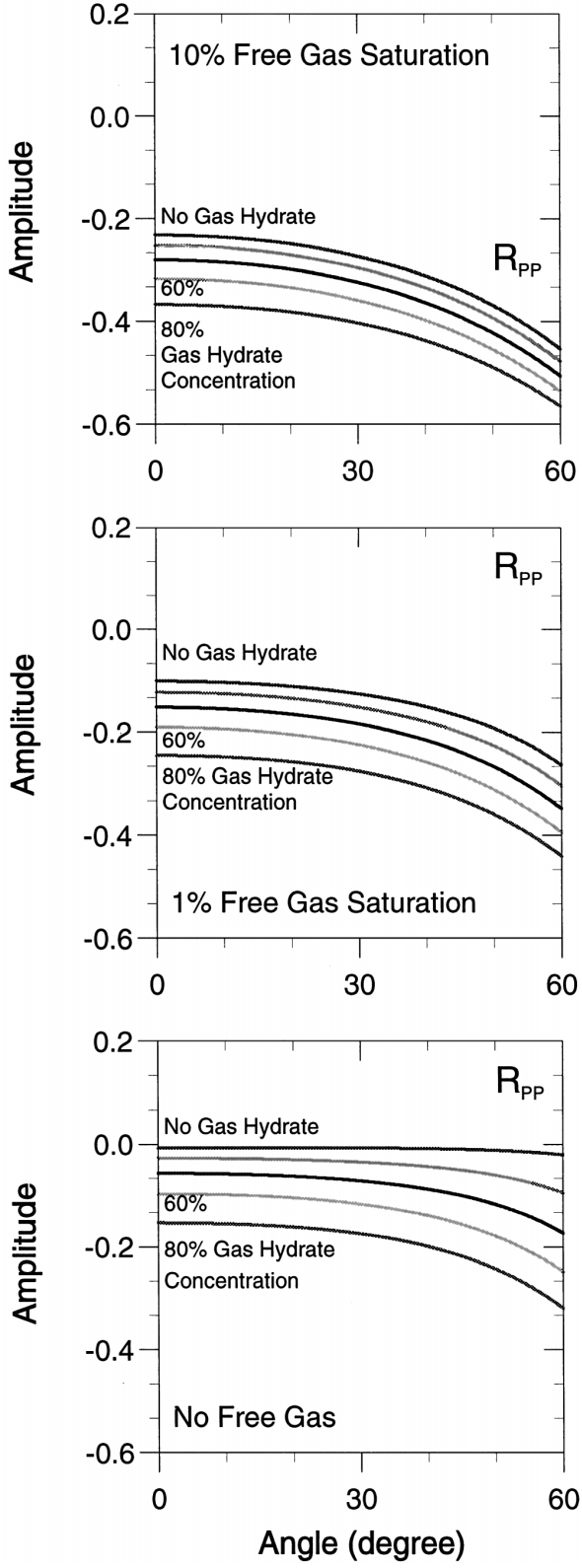


FIG. 8. Computed variations of BSR  $PP$ -wave viscoelastic reflection coefficient with angle of incidence for different free-gas and gas-hydrate saturations (LCA model without grain cementation).

The propagation effects due to attenuation can be observed in Figure 12, which shows CMP gathers of the vertical particle velocity for a BSR with 10% gas hydrate and 1% free gas in the lossy and lossless cases. Attenuation considerably affects the far-offset traces.

Finally, Figure 13 represents the reflection coefficients  $R_{PP}$ , phases, and interference coefficients corresponding to the bottom of the free gas zone (the frequency is 25 Hz). We assume that the quality factors of the free gas-bearing sediments are  $Q_1 = Q_2 = 20$ , and those of the water saturated sediment are  $Q_1 = Q_2 = 30$ . Small amounts of free gas can be determined from the amplitude strength, although all the saturations present the same type of anomaly. The interference between the incident and reflected  $P$ -waves is particularly high for all the saturations at far offsets. This indicates that much of the energy is lost by interference.

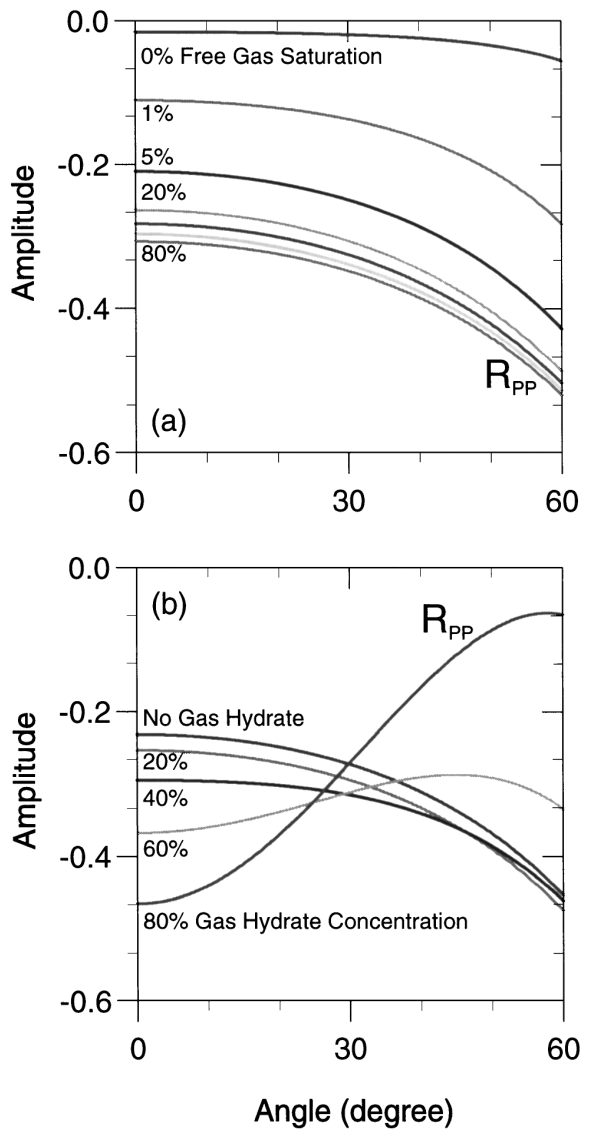


FIG. 9.  $PP$ -reflection coefficients versus incidence angle, calculated for sediments with 10% gas hydrate concentration (a) and 10% free-gas saturation (b).

## CONCLUSIONS

We model the wave velocities of gas hydrate–(ice-) and free gas-bearing sediments with three-phase Biot-type theories, and obtain the reflection coefficients for the top and base of a free gas layer, believed to be the cause of a BSR. Our conclusions are the following:

- 1) Grain cementation, simulated with a percolation model, is important for high concentrations of ice (gas hydrate).
- 2) Grain cementation and a porosimetric probability distribution are required for modeling permafrost velocities (in frozen Berea sandstone).
- 3) The model gives a nearly constant Poisson's ratio for low concentrations, and a rapidly decreasing one for high concentrations.

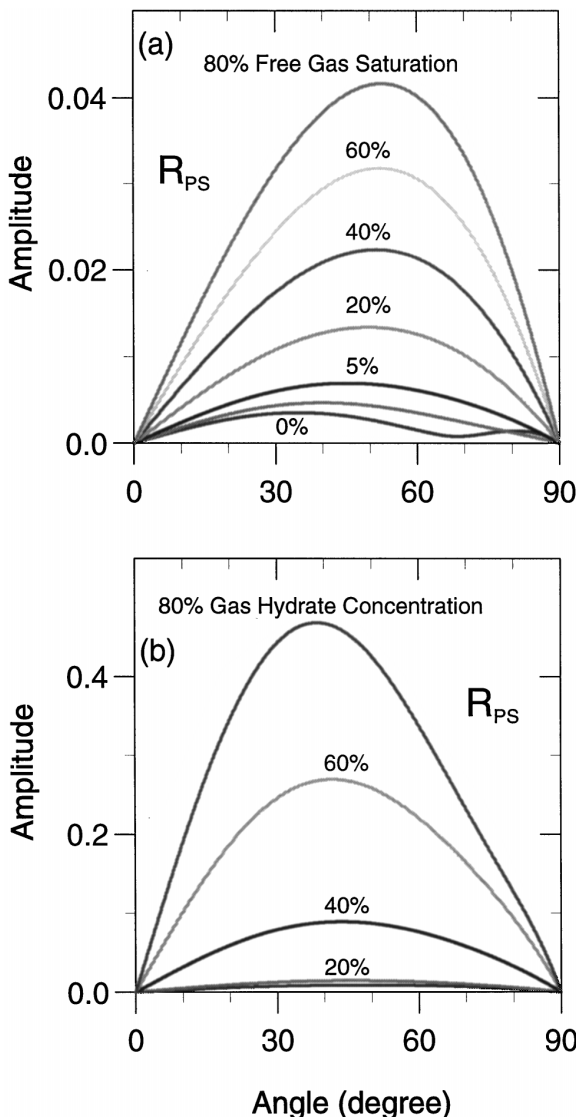


FIG. 10. PS-reflection coefficients versus incidence angle, calculated for sediments with 10% gas hydrate concentration (a) and 10% free gas saturation (b).

- 4) Small quantities of gas in the pore space cause a dramatic change in the amplitude of the compressional wave.
- 5) Increasing free gas saturation causes an increase in the magnitude of the near-offset reflection coefficient. However, for a given gas saturation, it is difficult to evaluate the amount of gas hydrate at low concentrations. For high concentrations, the AVO anomaly is negative.
- 6) The AVO anomaly is always positive when the grains are not cemented.

The curves show a strong positive anomaly for high concentrations of gas hydrate when the grains are uncemented. It is not possible to evaluate the amount of free gas, but the amount of gas hydrate can be determined from the AVO curves.

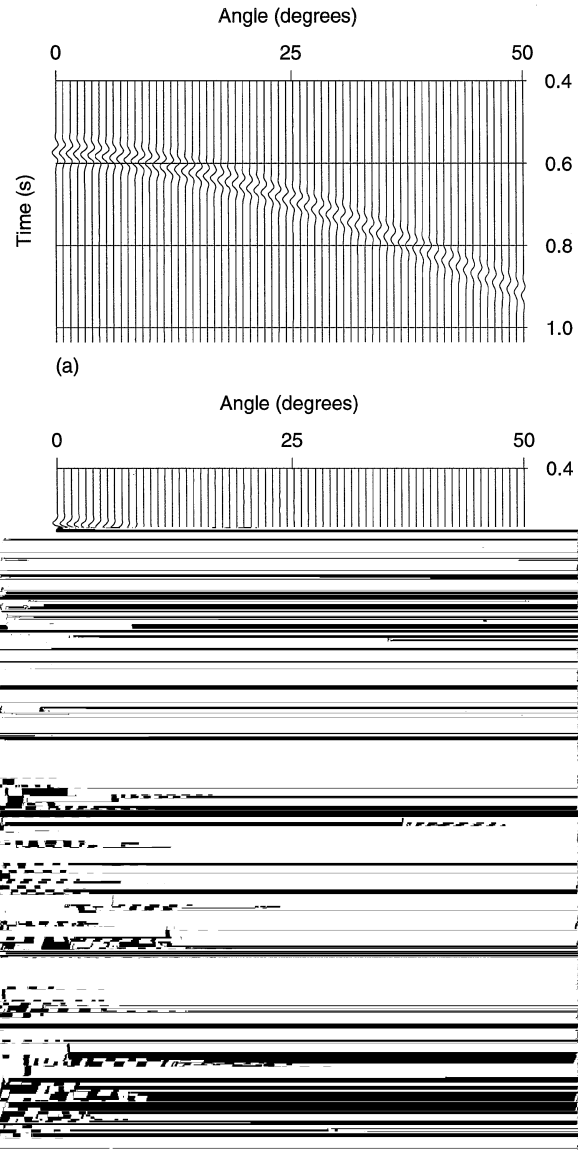


FIG. 11. CMP gathers of the vertical particle velocity for a BSR with 10% gas hydrate and (a) 0%, (b) 1%, and (c) 20% free gas. The material properties are given in Table 3.

- 7) The saturation of free gas can be determined from the reflection amplitude ( $R_{PP}$ ), but not from the type of anomaly.
- 8) The amount of gas hydrate can be determined when the concentration is high.
- 9) The  $P$  to  $S$  reflection coefficient is a good indicator of high amounts of free gas and gas hydrate.
- 10) Reflections from the base of the free gas zone indicate that small amounts of free gas can be determined from the amplitude strength, although all the saturations present the same type of anomaly. Moreover, the interference between the incident and reflected  $P$ -waves is particularly high for all the saturations at far offsets, indicating that much of the energy is lost by interference.
- 11) Propagation effects are important, since attenuation considerably affects the far-offsets traces.

Unlike in Biot's two-phase theory, the secondary (slow) waves are propagation modes in the seismic range. In particular, this occurs for high concentrations of gas hydrate. Then, events due to these waves may be present in the seismic records. If the free gas zone is thin compared to the dominant wavelength, the analysis requires a more complex AVO study taking into account the layer thickness. This is currently the subject of research using, for instance, a full wave modeling technique.

#### ACKNOWLEDGMENTS

This work was supported in part by Norsk Hydro a.s. (Bergen) and PNRA (Programma Nazionale di Ricerca in

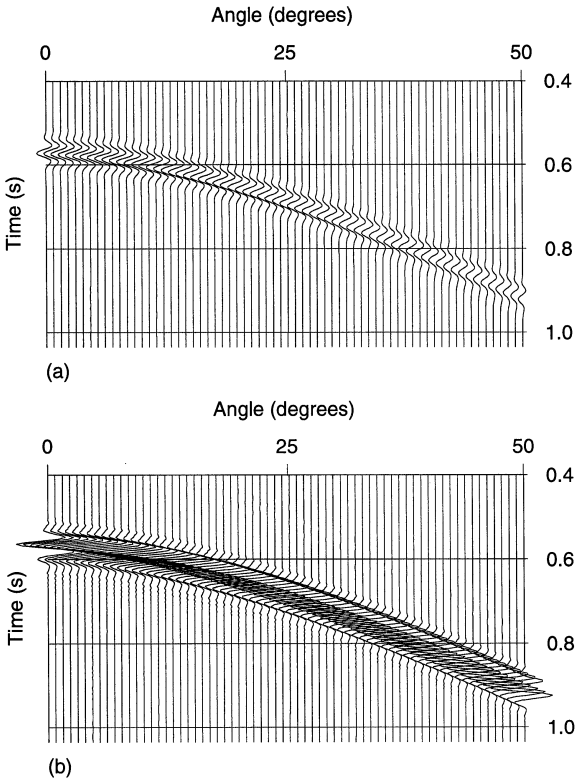


FIG. 12. CMP gathers of the vertical particle velocity for a BSR with 10% gas hydrate and 1% free gas in the lossy (a) and lossless (b) cases.

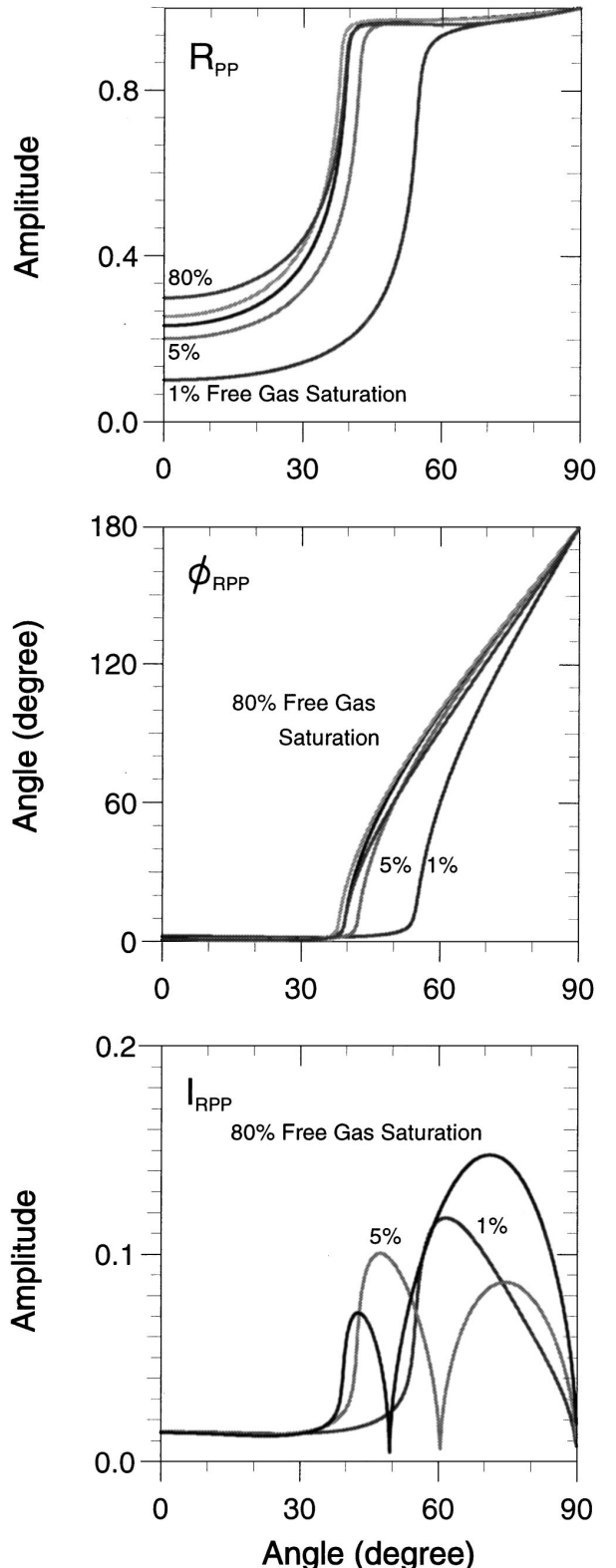


FIG. 13.  $PP$ -reflection coefficients, phases, and interference coefficients versus incidence angle for various free gas saturations. The interface corresponds to the bottom of the free gas zone.

Antartide). Thanks to Hans B. Helle for important technical comments.

## REFERENCES

- Andreassen, K., Hogstad, K., and Berteussen, K. A., 1990, Gas hydrate in the southern Barents Sea indicated by a shallow seismic anomaly: *First Break*, **8**, 235–245.
- Berryman, J. G., 1980, Confirmation of Biot's theory: *Appl. Phys. Lett.*, **37**, 382–384.
- Carcione, J. M., 1997, Reflection and transmission of  $qP$ - $qS$  plane waves at a plane boundary between viscoelastic transversely isotropic media: *Geophys. J. Internat.*, **129**, 669–880.
- Carcione, J. M., and Seriani, G., 1998, Seismic velocities in permafrost: *Geophys. Prosp.*, **46**, 441–454.
- Castagna, J. P., and Swan, H. W., 1997, Principles of AVO crossplotting: *The Leading Edge*, **16**, 337–342.
- Domenico, S. N., 1977, Elastic properties of unconsolidated porous sand reservoirs: *Geophysics*, **42**, 1339–1368.
- Ecker, C., Lumley, D., Dvorkin, J., and Nur, A., 1996, Structure of hydrates sediments from seismic and rock physics: 2nd Internat. Conf. on Natural Gas Hydrates, 491–498.
- Hudson, J., 1992, Surface science, an introduction: Butterworth-Heinemann.
- Leclaire, Ph., Cohen-Ténoudji, F., and Aguirre-Puente, J., 1994, Extension of Biot's theory of wave propagation to frozen porous media: *J. Acoust. Soc. Am.*, **96**, 3753–3768.
- Kuster, G. T., and Toksöz, M. N., 1974, Velocity and attenuation of seismic waves in two-phase media: Part I. Theoretical formulations: *Geophysics*, **39**, 587–606.
- Minshull, T. A., Singh, S. C., and Westbrook, G. K., 1994, Seismic velocity structure at a gas hydrate reflector, offshore western Colombia, from full waveform inversion: *J. Geophys. Res.*, **99**, B3, 4715–4734.
- ODP Leg 164 Shipboard Scientific Party, 1996, Methane gas hydrate drilled at Blake Ridge: *EOS*, **77**, no. 23.
- Reuss, A., 1929, Berechnung der Fleissgrenze von Mischkristallen auf Grund der Plastizitätsbelastung für ein Kristalle: *Z. Angew. Math. Mech.*, **9**, 49–58.
- Santos, J. E., Corberó, J., and Douglas, J., Jr., 1990a, Static and dynamic behaviour of a porous solid saturated by a two-phase fluid: *J. Acoust. Soc. Am.*, **87**, 1428–1438.
- Santos, J. E., Douglas, J., Jr., Corberó, J., and Lovera, O. M., 1990b, A model for wave propagation in a porous medium saturated by a two-phase fluid: *J. Acoust. Soc. Am.*, **87**, 1439–1448.
- Sloan, E. D., Jr., 1990, Clathrate hydrates of natural gases: Marcel Dekker.
- Timur, A., 1968, Velocity of compressional waves in porous media at permafrost temperatures: *Geophysics*, **33**, 584–595.
- Voigt, W., 1928, Lehrbuch der Kristallphysik: B. G. Teubner.
- Winkler, K. W., 1985, Dispersion analysis of velocity and attenuation in Berea sandstone: *J. Geophys. Res.*, **90**, B8, 6793–6800.
- Wood, A. B., 1941, A textbook of sound: G. Bell & Sons, Ltd.
- Zimmerman, R. W., and King, M. S., 1986, The effect of the extent of freezing on seismic velocities in unconsolidated permafrost: *Geophysics*, **39**, 587–606.

## APPENDIX A

### LIST OF SYMBOLS

#### Model for ice (gas hydrate)-bearing sediments

$a_{12}$	tortuosity for water flowing through the solid matrix
$a_{13}$	tortuosity for solid flowing through the ice matrix
$a_{23}$	tortuosity for water flowing through the ice matrix
$a_{31}$	tortuosity for ice flowing through the solid matrix
$b_{11}$	$= \eta_D \phi_w^2 / \kappa_s$
$b_{33}$	$= \eta_D \phi_w^2 / \kappa_i$
$c_1$	consolidation coefficient for the solid: $K_{sm} / \phi_s K_s$
$c_3$	consolidation coefficient for the ice: $K_{im} / \phi_i K_i$
$\text{Re}[F(\xi)]$	$= 1 + (1/0.7178) \exp[0.7178(\xi - 3.2)]/12$ , if $\xi \leq 3.2$
$\text{Re}[F(\xi)]$	$= 0.5 + \{2\xi + \exp[-0.7178(\xi - 3.2)]\}/12$ , if $\xi > 3.2$
$\text{Im}[F(\xi)]$	$= \xi/6$
$g_1$	consolidation coefficient for the solid: $\mu_{sm} / \phi_s \mu_s$
$g_3$	consolidation coefficient for the ice: $\mu_{im} / \phi_i \mu_i$
$h$	average thickness of the water layer $= r_s [(1 + \phi_w / \phi_s)^{1/3} - 1]$
$K_s$	solid bulk modulus
$K_w$	water bulk modulus
$K_i$	ice bulk modulus
$K_{sm}$	bulk modulus of the matrix formed by the solid phase
$K_{\max}$	Kuster-Toksöz's bulk modulus for the ice matrix
$K_{im}$	bulk modulus of the matrix formed by the ice $= K_{\max} [\phi_i / (1 - \phi_s)]^{3.8}$
$K_{av}$	average bulk modulus: $[(1 - c_1)\phi_s / K_s + \phi_w / K_w + (1 - c_3)\phi_i / K_i]^{-1}$ $= K_1 + 4\mu_{11}/3 = [(1 - c_1)\phi_s]^2 K_{av} + K_{sm} + 4\mu_{11}/3$
$R_{11}$	$= C_{12} = (1 - c_1)\phi_s \phi_w K_{av}$
$R_{12}$	$= C_{13} + 2\mu_{13}/3 = (1 - c_1)(1 - c_3)\phi_s \phi_i K_{av} + 2\mu_{13}/3$
$R_{13}$	$= \phi_w^2 K_{av}$
$R_{22}$	$= C_{23} = (1 - c_3)\phi_i \phi_w K_{av}$
$R_{23}$	$= K_3 + 4\mu_{33}/3 = [(1 - c_3)\phi_i]^2 K_{av} + K_{im} + 4\mu_{33}/3$
$R_{33}$	geometrical aspect of the boundary separating solid from water

$r_{13}$	geometrical aspect of the boundary separating solid from ice
$r_{23}$	geometrical aspect of the boundary separating ice from water
$r_{31}$	geometrical aspect of the boundary separating ice from solid
$r_s$	average radius of solid grains
$r_{av}$	average radius of the capillary pore
$S_i$	ice concentration: $\phi_i / (\phi_i + \phi_w)$
$T$	water temperature in degrees Celsius
$\Delta r$	standard deviation of the capillary pore
$\bar{\eta}_w$	viscosity of free water: $1.798 \cdot 10^{-3}$ $\exp(-0.03753T)$ , $-20^\circ\text{C} < T < 0^\circ\text{C}$
$10 \log_{10} \bar{\eta}_w$	$= 1301/[998.333 + 8.1855(T - 20) + 0.00585(T - 20)^2] - 3.30233$ , $0^\circ\text{C} < T < 20^\circ\text{C}$ , viscosity of interstitial water: $\bar{\eta}_w(450 + h)/h$ , with $h$ in angstroms
$\eta_w$	dynamical viscosity of interstitial water: $\eta_w F(\xi)$
$\eta_D$	solid matrix permeability
$\kappa_{s0}$	ice matrix permeability
$\kappa_{i0}$	$= \kappa_{s0} \phi_w^3 / (1 - \phi_s)^3$
$\kappa_s$	$= \kappa_{i0} [(1 - \phi_s) / \phi_i]^2 (\phi_w / \phi_s)^3$
$\kappa_i$	solid shear modulus
$\mu_s$	ice shear modulus
$\mu_i$	Kuster-Toksöz's shear modulus for the solid matrix
$\mu_{smKT}$	solid matrix shear modulus: $[\mu_{smKT} - \mu_{sm0}] [\phi_i / (1 - \phi_s)]^{3.8} + \mu_{sm0}$
$\mu_{sm}$	Kuster-Toksöz's shear modulus for the ice matrix
$\mu_{\max}$	shear modulus of the matrix formed by the ice
$\mu_{im}$	$= \mu_{\max} [\phi_i / (1 - \phi_s)]^{3.8}$
$\mu_{av}$	average shear modulus: $[(1 - g_1)\phi_s / \mu_s + \phi_w / i\omega\eta_w + (1 - g_3)\phi_i / \mu_i]^{-1}$
$\mu_{11}$	$= [(1 - g_1)\phi_s]^2 \mu_{av} + \mu_{sm}$
$\mu_{13}$	$= (1 - g_1)(1 - g_3)\phi_s \phi_i \mu_{av} + \hat{\mu}_{si}$
$\mu_{33}$	$= [(1 - g_3)\phi_i]^2 \mu_{av} + \mu_{im}$

$\mu_{si}$	coupling shear modulus between the ice and solid phases	$\bar{g}_2$	$= S_w \rho_w F_s / (\phi_g + \phi_w)$
$\omega$	angular frequency: $2\pi f$	$\bar{g}_3$	$= 0.1 \sqrt{\bar{g}_1 \bar{g}_2}$
$\phi_s$	proportion of solid	$K_s$	gas bulk modulus
$\phi_w$	proportion of water	$K_c$	$= K_s (K_{sm} + Q) (K_s + Q)$
$\phi_i$	proportion of ice	$K_f$	$= \alpha / (\gamma S_g / K_g + S_w / K_w)$
$\rho_s$	solid density	$M_1$	$= B_2 r / q$
$\rho_w$	water density	$M_2$	$= -B_1 / (K_{sm} \delta) - M_3$
$\rho_i$	ice density	$M_3$	$= -B_2 [1 / (K_{sm} \delta) + r / q]$
$\rho_{11}$	$= \phi_s \rho_s a_{13} + (a_{12} - 1) \phi_w \rho_w + (a_{31} - 1) \phi_i \rho_i - i b_{11} / \omega$	$p_c$	capillary pressure: $2650.9 e^{-3.1291} (e^{-6.029158 S_g} - 1)$
$\rho_{12}$	$= -(a_{12} - 1) \phi_w \rho_w + i b_{11} / \omega$	$Q$	$= K_f (K_{sm} - K_s) / [(K_f - K_s) (\phi_w + \phi_g)]$
$\rho_{13}$	$= -(a_{13} - 1) \phi_s \rho_s - (a_{31} - 1) \phi_i \rho_i$	$q$	$= (\phi_g + \phi_w) [1 / K_g + 1 / (S_g S_w \partial p_c / \partial S_g)]$
$\rho_{22}$	$= (a_{12} + a_{23} - 1) \phi_w \rho_w - i (b_{11} + b_{33}) / \omega$	$r$	$= (S_g + \beta) / K_s + \chi / K_{sm}$
$\rho_{23}$	$= -(a_{23} - 1) \phi_w \rho_w + i b_{33} / \omega$	$S_g$	gas saturation: $\phi_g / (\phi_g + \phi_w)$
$\rho_{33}$	$= \phi_i \rho_i a_{31} + (a_{23} - 1) \phi_w \rho_w + (a_{13} - 1) \phi_s \rho_s - i b_{33} / \omega$	$S_w$	water saturation: $\phi_w / (\phi_g + \phi_w)$
$\xi$	$= (h/2) (\omega \rho_w / \eta_w)^{1/2}$	$\alpha$	$= (\gamma - 1) (S_g + \beta) + 1$
		$\beta$	$= p_c / (\partial p_c / \partial S_g)$
		$\delta$	$= 1 / K_s - 1 / K_{sm}$
		$\gamma$	$= [1 + S_g S_w (\partial p_c / \partial S_g) / K_w] / [1 + S_g S_w (\partial p_c / \partial S_g) / K_g]$
		$\rho_g$	gas density
		$\rho_m$	mass density of the bulk material: $\phi_s \rho_s + \phi_g \rho_g + \phi_w \rho_w$
		$\phi_g$	proportion of gas
		$\Theta$	$= \frac{\delta + (\phi_g + \phi_w)(1/K_{sm} - 1/K_f)}{\alpha[\delta + (\phi_g + \phi_w)(1/K_{sm} - 1/K_f)]}$

### Model for free gas-bearing sediments

$$\begin{aligned} B_1 &= K_c \Theta [(S_g + \beta) \gamma - \beta] \\ B_2 &= K_c \Theta S_w \\ F_s &= \text{structure factor: 2.8} \\ \bar{g}_1 &= S_g \rho_g F_s / (\phi_g + \phi_w) \end{aligned}$$

### APPENDIX B

#### EXTENSION OF LECLAIRE ET AL.'S THEORY

Leclaire et al. (1994) assume that there is no direct mechanical contact between solid and ice. The model is generalized here in order to include this interaction. Following Leclaire et al.'s notation,  $u_v$ ,  $v = 1, \dots, 3$  denote the displacement vectors of solid, water, and ice, respectively.

#### Potential energy density

The total potential energy of the system can be expressed as

$$\mathbf{V} = \mu_{11} d_1^2 + \frac{1}{2} K_1 \theta_1^2 + C_{12} \theta_1 \theta_2 + \frac{1}{2} K_2 \theta_2^2 + C_{23} \theta_2 \theta_3 + \frac{1}{2} K_3 \theta_3^2 + \mu_{33} d_3^2 + C_{13} \theta_1 \theta_3 + \mu_{13} D, \quad (\text{B-1})$$

where  $\theta_v$  and  $d_v$  are the invariants of the strain tensor, called deviators and dilatations,  $D = d_{ij}^{(1)} d_{ij}^{(3)}$ , with  $d_{ij}^{(v)}$  the deviator tensor,  $K_v$  and  $\mu_{vv'}$  are, respectively, the bulk and shear moduli of the effective phases. Note that since  $D$  is the trace of the scalar product between the vectors  $d^{(1)}$  and  $d^{(3)}$ , it is an invariant quantity.

All the parameters except  $C_{13}$  and  $\mu_{13}$  are given in Leclaire et al. (1994). However, they are not modified by solid/ice interactions. In order to calculate  $C_{13}$ , and  $\mu_{13}$ , we generalize the elastic moduli obtained for the two-phase Biot's theory. For a medium with a solid porosity  $\phi_s$  and a fluid porosity  $\phi_f$ , the elastic moduli are

$$\begin{aligned} K_1 &= (1 - c_1)^2 \phi_s^2 K_a, \\ C_{12} &= (1 - c_1) \phi_s \phi_f K_a, \\ K_2 &= \phi_f^2 K_a, \\ K_a &= \left[ (1 - c_1) \frac{\phi_s}{K_s} + \frac{\phi_f}{K_f} \right]^{-1}, \quad c_1 = \frac{K_{sm}}{\phi_s K_s}, \end{aligned} \quad (\text{B-2})$$

where  $K_s$  and  $K_f$  are the solid and fluid bulk moduli,  $K_a$  is the average bulk modulus,  $K_{sm}$  is the solid matrix bulk modulus, and  $c_1$  is the bulk consolidation coefficient such that  $c_1 = 0$  for a suspension of solid grains in a fluid and  $c_1 = 1$  for a situation where the grains form a monolithic block. Note that equations (B-2) correspond to an effective solid porosity  $\phi'_s = (1 - c_1) \phi_s$ . If we replace ice by water, the equations should read

$$\begin{aligned} K_1 &= \phi'_s^2 K_a, \\ C_{13} &= \phi'_s \phi_i K_a, \\ K_3 &= \phi'_i^2 K_a, \\ K_a &= \left[ \frac{\phi'_s}{K_s} + \frac{\phi'_i}{K_i} \right]^{-1}, \quad c_3 = \frac{K_{im}}{\phi_i K_i}, \end{aligned} \quad (\text{B-3})$$

where  $c_3$  is the bulk consolidation coefficient of the ice matrix with bulk modulus  $K_{im}$ . For the three-phase system, generalization of  $K_a$  to

$$K_{av} = \left[ \frac{\phi'_s}{K_s} + \frac{\phi'_i}{K_i} + \frac{\phi_w}{K_w} \right]^{-1}$$

gives

$$\begin{aligned} K_1 &= (1 - c_1)^2 \phi_s^2 K_{av}, \\ C_{13} &= (1 - c_1) \phi_s (1 - c_3) \phi_i K_{av}, \\ K_3 &= (1 - c_3)^2 \phi_i^2 K_{av}, \\ K_{av} &= \left[ (1 - c_1) \frac{\phi_s}{K_s} + (1 - c_3) \frac{\phi_i}{K_i} + \frac{\phi_w}{K_w} \right]^{-1}. \end{aligned} \quad (\text{B-4})$$

The shear modulus  $\mu_{13}$ , given in appendix A, has an analogous expression to that of  $C_{13}$ .

### Kinetic energy density

The kinetic energy is a function of the local velocities  $\dot{u}_1, \dot{u}_2$ , and  $\dot{u}_3$ , where the dot denotes time differentiation. Generalizing Leclaire et al.'s kinetic energy, we get

$$\mathbf{C} = \frac{1}{2}\rho_{11}\dot{u}_1^2 + \frac{1}{2}\rho_{22}\dot{u}_2^2 + \frac{1}{2}\rho_{33}\dot{u}_3^2 + \rho_{12}\dot{u}_1\dot{u}_2 + \rho_{23}\dot{u}_2\dot{u}_3 + \rho_{13}\dot{u}_1\dot{u}_3, \quad (\text{B-5})$$

where, for simplicity, we omit the tilde above the density components.

Let us define the macroscopic velocities

$$\dot{w}_1 = \phi_w(\dot{u}_2 - \dot{u}_1) \quad \text{and} \quad \dot{w}_3 = \phi_w(\dot{u}_2 - \dot{u}_3), \quad (\text{B-6})$$

characterizing water-solid and water-ice flow, and

$$\dot{q} = \phi_i(\dot{u}_3 - \dot{u}_1) \quad \text{and} \quad \dot{r} = \phi_s(\dot{u}_1 - \dot{u}_3), \quad (\text{B-7})$$

the macroscopic velocity characterizing the flow of ice relative to the solid phase and vice versa, respectively. Since the relative flow is assumed to be of laminar type, the microscopic velocities can be expressed as

$$v_1 = \alpha_{ij}^{(1)}(\dot{w}_j)_1 \quad \text{and} \quad v_3 = \alpha_{ij}^{(3)}(\dot{w}_j)_3, \quad (\text{B-8})$$

and

$$s = \beta_{ij}^{(1)}\dot{q}_j \quad \text{and} \quad t = \beta_{ij}^{(3)}\dot{r}_j, \quad (\text{B-9})$$

where  $\alpha_{ij}^{(1)}$  and  $\alpha_{ij}^{(3)}$  are the water/solid and water/ice coefficients, and  $\beta_{ij}^{(1)}$  and  $\beta_{ij}^{(3)}$  the ice/solid and solid/ice coefficients, respectively.

The total kinetic energy is given by the expression

$$\begin{aligned} \mathbf{C} = & \frac{1}{2}\rho_w \iiint_{\Omega_w} (\dot{u}_1 + v_1)^2 d\Omega \\ & + \frac{1}{2}\rho_w \iiint_{\Omega_w} (\dot{u}_3 + v_3)^2 d\Omega - \frac{1}{2}\rho_w \phi_w \dot{u}_2^2 \\ & + \frac{1}{2}\rho_i \iiint_{\Omega_i} (\dot{u}_1 + s)^2 d\Omega \\ & + \frac{1}{2}\rho_s \iiint_{\Omega_s} (\dot{u}_3 + t)^2 d\Omega, \end{aligned} \quad (\text{B-10})$$

where  $\Omega_w$ ,  $\Omega_i$ , and  $\Omega_s$  are the volumes of water, ice, and solid, respectively. The term  $(1/2)\rho_w \phi_w \dot{u}_2^2$  is subtracted since the contribution of water must be considered only once in the kinetic energy.

Following Leclaire et al. (1994), defining

$$(m_{ij})_\ell \equiv \rho_w \iiint_{\Omega'} \sum_k \alpha_{ki}^{(\ell)} \alpha_{kj}^{(\ell)} d\Omega, \quad \ell = 1, 3 \quad (\text{B-11})$$

and

$$\begin{aligned} (n_{ij})_1 & \equiv \rho_i \iiint_{\Omega'} \sum_k \beta_{ki}^{(1)} \beta_{kj}^{(1)} d\Omega, \\ (n_{ij})_3 & \equiv \rho_s \iiint_{\Omega'} \sum_k \beta_{ki}^{(3)} \beta_{kj}^{(3)} d\Omega, \end{aligned} \quad (\text{B-12})$$

where  $\Omega'$  is the volume of the flowing phases, and assuming statistical isotropy, we obtain

$$\begin{aligned} \mathbf{C} = & \frac{1}{2}\rho_2\dot{u}_1^2 + \rho_w\dot{u}_1\dot{w}_1 + \frac{1}{2}m_1\dot{w}_1^2 + \frac{1}{2}\rho_2\dot{u}_3^2 + \rho_w\dot{u}_3\dot{w}_3 \\ & + \frac{1}{2}m_3\dot{w}_3^2 - \frac{1}{2}\rho_w\phi_w\dot{u}_2^2 + \frac{1}{2}\rho_3\dot{u}_1^2 + \rho_i\dot{u}_1\dot{q} + \frac{1}{2}n_1\dot{q}^2 \\ & + \frac{1}{2}\rho_1\dot{u}_3^2 + \rho_s\dot{u}_3\dot{r} + \frac{1}{2}n_3\dot{r}^2, \end{aligned} \quad (\text{B-13})$$

where

$$\rho_1 = \rho_s\phi_s, \quad \rho_2 = \rho_w\phi_w, \quad \rho_3 = \rho_i\phi_i.$$

Finally, expressing the kinetic energy as a function of  $\dot{u}_1, \dot{u}_2$ , and  $\dot{u}_3$ , we get

$$\begin{aligned} \mathbf{C} = & \frac{1}{2}(n_3\phi_s^2 - \rho_2 + m_1\phi_w^2 - \rho_3 + n_1\phi_i^2)\dot{u}_1^2 \\ & + \frac{1}{2}(m_1\phi_w^2 + m_3\phi_w^2 - \rho_2)\dot{u}_2^2 \\ & + \frac{1}{2}(n_1\phi_i^2 - \rho_2 + m_3\phi_w^2 - \rho_1 + n_3\phi_s^2)\dot{u}_3^2 \\ & + (\rho_2 - m_1\phi_w^2)\dot{u}_1\dot{u}_2 + (\rho_2 - m_3\phi_w^2)\dot{u}_2\dot{u}_3 \\ & + (\rho_1 - n_3\phi_s^2 + \rho_3 - n_1\phi_i^2)\dot{u}_1\dot{u}_3. \end{aligned} \quad (\text{B-14})$$

The generalized mass densities  $\rho_{ij}$  are obtained by equating the coefficients of expression (B-14) with those of equation (B-5). Thus

$$\begin{aligned} \rho_{11} & = \rho_s\phi_s a_{13} + (a_{12} - 1)\rho_w\phi_w + (a_{31} - 1)\rho_i\phi_i, \\ \rho_{22} & = (a_{12} + a_{23} - 1)\rho_w\phi_w, \\ \rho_{33} & = \rho_i\phi_i a_{31} + (a_{23} - 1)\rho_w\phi_w + (a_{13} - 1)\rho_s\phi_s, \\ \rho_{12} & = -(a_{12} - 1)\rho_w\phi_w, \\ \rho_{23} & = -(a_{23} - 1)\rho_w\phi_w, \\ \rho_{13} & = -(a_{13} - 1)\rho_s\phi_s - (a_{31} - 1)\rho_i\phi_i, \end{aligned} \quad (\text{B-15})$$

where

$$a_{12} = \frac{m_1\phi_w}{\rho_w}, \quad a_{23} = \frac{m_3\phi_w}{\rho_w}, \quad (\text{B-16})$$

and

$$a_{13} = \frac{n_3\phi_s}{\rho_s}, \quad a_{31} = \frac{n_1\phi_i}{\rho_i} \quad (\text{B-17})$$

are the tortuosity parameters.

When there is no relative motion between the three phases, the following relation holds

$$\rho = \rho_{11} + \rho_{22} + \rho_{33} + 2\rho_{12} + 2\rho_{23} + 2\rho_{13} = \rho_1 + \rho_2 + \rho_3, \quad (\text{B-18})$$

corresponding to the effective mass density.

Following Berryman (1980) and Leclaire et al. (1994), we express the tortuosity parameters as

$$\begin{aligned} a_{12} &= \frac{\phi_s \rho}{\phi_w \rho_w} r_{12} + 1, & a_{23} &= \frac{\phi_i \rho'}{\phi_w \rho_w} r_{23} + 1, \\ a_{13} &= \frac{\phi_i \rho'}{\phi_s \rho_s} r_{13} + 1, & a_{31} &= \frac{\phi_s \rho}{\phi_i \rho_i} r_{31} + 1, \end{aligned} \quad (\text{B-19})$$

where

$$\rho = \frac{\phi_w \rho_w + \phi_i \rho_i}{\phi_w + \phi_i}, \quad \rho' = \frac{\phi_w \rho_w + \phi_s \rho_s}{\phi_w + \phi_s},$$

and  $r_{vv'}$  characterize the geometrical features of the pores ( $r=1/2$  for spheres). This approximation is based on the fact that the three phases are mechanically decoupled. Observe that, for instance,  $a_{12} \rightarrow 1$  for  $\phi_w \rightarrow 1$  and that  $a_{12} \rightarrow \infty$  for  $\phi_w \rightarrow 0$ , as expected (Berryman, 1980).